A Genome-Scale Metabolic Model Accurately Predicts Fluxes in Central Carbon Metabolism under Stress Conditions[1][C][W]

Thomas C.R. Williams, Mark G. Poolman, Andrew J.M. Howden, Markus Schwarzlander, David A. Fell, R. George Ratcliffe, and Lee J. Sweetlove*

Department of Plant Sciences, University of Oxford, Oxford OX1 3RB, United Kingdom (T.C.R.W., A.J.M.H., M.S., R.G.R., L.J.S.); and School of Life Science, Oxford Brookes University, Headington, Oxford OX3 OBP, United Kingdom (M.G.P., D.A.F.)

Flux is a key measure of the metabolic phenotype. Recently, complete (genome-scale) metabolic network models have been established for Arabidopsis (*Arabidopsis thaliana*), and flux distributions have been predicted using constraints-based modeling and optimization algorithms such as linear programming. While these models are useful for investigating possible flux states under different metabolic scenarios, it is not clear how close the predicted flux distributions are to those occurring in vivo. To address this, fluxes were predicted for heterotrophic Arabidopsis cells and compared with fluxes estimated in parallel by ^{13}C-metabolic flux analysis (MFA). Reactions of the central carbon metabolic network (glycolysis, the oxidative pentose phosphate pathway, and the tricarboxylic acid [TCA] cycle) were independently analyzed by the two approaches. Net fluxes in glycolysis and the TCA cycle were predicted accurately from the genome-scale model, whereas the oxidative pentose phosphate pathway was poorly predicted. MFA showed that increased temperature and hyperosmotic stress, which altered cell growth, also affected the intracellular flux distribution. Under both conditions, the genome-scale model was able to predict both the direction and magnitude of the changes in flux: namely, increased TCA cycle and decreased phospho*enol*pyruvate carboxylase flux at high temperature and a general decrease in fluxes under hyperosmotic stress. MFA also revealed a 3-fold reduction in carbon-use efficiency at the higher temperature. It is concluded that constraints-based genome-scale modeling can be used to predict flux changes in central carbon metabolism under stress conditions.

As most of the uses of plants are intimately linked to their metabolic output or activity, there is a renewed interest in understanding the behavior and regulation of plant metabolic networks. The only direct measure of metabolic activity, and the facet most closely related to biological function, is flux through the metabolic network (Libourel and Shachar-Hill, 2008). There has been a considerable research effort in the last few years to develop and refine methods that allow fluxes in large metabolic networks to be determined. The best established of these methods, steady-state metabolic flux analysis (MFA), involves measuring the redistribution of a supplied stable isotope, usually ^{13}C, at metabolic and isotopic steady state (Ratcliffe and Shachar-Hill, 2006; Allen et al., 2009a). Flux maps of a range of heterotrophic plant cells and tissues have

been produced, providing information on the operation of different flux modes (Sriram et al., 2004, 2007; Schwender et al., 2006; Allen et al., 2009b; Masakapalli et al., 2010), carbon-use efficiency (Alonso et al., 2007), and the response of the network to different substrates (Junker et al., 2007), altered genotype (Lonien and Schwender, 2009), and altered growth conditions (Iyer et al., 2008; Williams et al., 2008). While MFA is currently the most powerful way to estimate metabolic network fluxes, allowing estimation of both net and exchange fluxes within subcellular compartments, there remain some technical issues that prevent a more routine exploitation of the method. In particular, the need to supply a labeled organic carbon substrate to isotopic steady state limits the tissue types that can be investigated, and the technique is also relatively low throughput (Kruger and Ratcliffe, 2009).

A complementary approach is provided by constraints-based modeling (Reed and Palsson, 2003; Borodina and Nielsen, 2005). In this approach, more routinely accessible experimental parameters, such as growth rate, substrate consumption rate, and biomass composition, are used to constrain the flux solution space within a network of defined reactions at steady state. The use of optimization algorithms, typically linear programming, can identify flux solutions that optimize an objective function such as maximization of growth or minimization of fluxes. This approach

was used to predict fluxes in a network of 257 reactions of primary metabolism in barley (*Hordeum vulgare*) seeds (Grafahrend-Belau et al., 2009). Because the method can handle very large networks, it can also be used to tackle metabolic networks on a genome scale, and this has been achieved for Arabidopsis (*Arabidopsis thaliana*; Poolman et al., 2009; de Oliveira Dal'Molin et al., 2010). These studies have provided new insight into metabolic network behavior, have identified variable flux modes within the network, both known and novel, and have allowed the behavior of the system under altered conditions to be explored, such as altered energy demand and altered oxygen availability.

The constraints-based modeling approach is attractive because of its speed and flexibility. Although the initial building of a genome-scale model is time consuming, once a stoichiometrically balanced network has been established it is relatively easy to explore a variety of metabolic scenarios. Moreover, with appropriate experimental data, the model can be used to predict the metabolic state of any plant tissue that can be assumed to operate at metabolic steady state, including autotrophic tissues (de Oliveira Dal'Molin et al., 2010). Specific models for specific cell and tissue types can be generated using transcript or protein expression data to define the enzymes present (Becker and Palsson, 2008). It is also possible to vary the objective function of the optimization routine to explore the factors that shape the structure and function of the network (Schuetz et al., 2007).

However, there are a number of potential problems in the interpretation of the results generated by such methods. First, the networks tend to be highly underdetermined, resulting in the strong possibility of multiple solutions. Although this can be addressed by the use of nonlinear objective functions (Grafahrend-Belau et al., 2009), it remains unclear how well parallel reactions and substrate cycles can be resolved. Second, thermodynamic constraints on reactions are only represented as simple reversible/irreversible criteria and hence only crudely represent in vivo free energy changes. Finally, the extent to which the actual biological optimization of a particular metabolic network can be represented by relatively simple objective functions has only been tested for single-celled microorganisms (Schuetz et al., 2007). Hence, the aim of the work presented in this paper was to establish how well fluxes predicted from analysis of a constraints-based genome-scale model reflect the real flux distribution. To this end, flux solutions for heterotrophic Arabidopsis cells were generated from a genome-scale model of Arabidopsis and compared with fluxes determined by ^{13}C-based MFA. Importantly, all the experimental data used in the two approaches were determined in parallel on the same batch of cells. As well as optimal growth conditions, the cells were also cultured under two stress conditions, increased temperature and hyperosmotic stress, to examine how well the changes in metabolic network fluxes could be predicted

from the constraints-based model. This work also revealed important new insights into the metabolic response to these two agriculturally relevant stress conditions.

RESULTS

Prediction of Fluxes in Heterotrophic Arabidopsis Cells Using a Genome-Scale Metabolic Model

The aim of this work was to compare the flux solution for a heterotrophic Arabidopsis cell suspension predicted from a genome-scale metabolic model (Poolman et al., 2009) with that estimated from ^{13}C-MFA (Williams et al., 2008; Masakapalli et al., 2010). Arabidopsis cells in heterotrophic culture provide a convenient system to investigate the fundamentals of heterotrophic metabolic behavior (Poolman et al., 2009). To provide a sound basis for comparison, all experimental parameters were measured in parallel on the same batch of cell suspension cultures after 5 d of growth. For the genome-scale model, experimental data consisted of growth rate, Glc consumption rate, and biomass composition (Table I). The values for these parameters were similar to those reported previously (Poolman et al., 2009). The most abundant soluble metabolites were also quantified and found to account for 14% of biomass. The abundance of individual metabolites is shown in Table II.

These data were used to constrain fluxes in a genome-scale metabolic model as described previously (Poolman et al., 2009). Briefly, the rate of growth and the composition of the biomass were used to derive constraints on the rates of synthesis of different biomass precursors, and linear programming was used to identify a flux solution with the objective of minimizing total flux. To account for the energy demand above that required for biomass synthesis (i.e. cell maintenance), a generic ATPase reaction was added to the model and the flux through this reaction varied until the Glc consumption rate in the model solution matched that observed experimentally. Soluble metabolites were included as constraints by assuming that their net rate of synthesis could be calculated from their abundance and the rate of biomass accumulation. This assumption is reasonable for abundant metabolites that predominantly accumulate in the vacuole (Farre et al., 2001) and are unlikely to be subject to appreciable rates of turnover. Glc content was not included as a constraint due to the possibility of contamination from the growth medium. The amino acid composition of protein was assumed to be the same as before (Poolman et al., 2009), and this was confirmed by measurement of a subset of protein amino acids by gas chromatography-mass spectrometry (GC-MS; data not shown). The model is available at http://mudshark.brookes.ac.uk/Models/Arabidopsis, and the complete flux solution is shown in Supplemental Table S1.

Table I. *Growth rate (biomass accumulation), Glc consumption rate, and biomass composition of Arabidopsis cell suspension cultures grown under control conditions (21°C, no mannitol), at high temperature (29°C), and under hyperosmotic stress (171 mM mannitol)*

All values are means ± SD from four replicates. Values indicated in boldface are significantly different (Student's t test, $P < 0.05$) from the corresponding value for control cells.

Parameter	Control	29°C	Hyperosmotic
Biomass (g dry wt d^{-1} L^{-1} culture)	2.3 ± 0.1	**0.8 ± 0.1**	**0.9 ± 0.2**
Glc consumption (g d^{-1} L^{-1} culture)	4.1 ± 0.2	**3.3 ± 0.1**	**1.6 ± 0.5**
Biomass composition (%)			
Cell wall	43 ± 5	35 ± 2	**55 ± 2**
Protein	20 ± 2	**16 ± 3**	**28 ± 4**
Lipid	11 ± 2	10 ± 1	11 ± 2
Starch	5 ± 0.4	**3 ± 0.4**	5 ± 0.7
Soluble metabolites	14 ± 1	21 ± 1	**7 ± 1**

Estimation of Fluxes in Heterotrophic Arabidopsis Cells from ^{13}C- MFA

A parallel batch of cell suspensions was supplied with [1-^{13}C]Glc, and the redistribution of ^{13}C in soluble metabolites was measured using GC-MS. GC-MS was also used to analyze labeling of amino acids from hydrolyzed protein and of Glc and maltose from starch. Metabolic fluxes were estimated using 13C-FLUX (Wiechert et al., 2001), and the flux solution was constrained with the same substrate uptake rate and biomass component accumulation rates as the genome-scale model (Tables I and II). The metabolic network used to fit the ^{13}C data (Fig. 1) was essentially the same as the one described by Williams et al. (2008), but with minor modifications to account for the difference in ^{13}C data (GC-MS versus NMR). For example, during analysis of Suc by GC-MS, it was not possible to distinguish MS fragments arising from the glucosyl and fructosyl moiety; therefore, labeling data from Fru, Glc, and Suc were assigned to a single cytosolic hexose phosphate pool. This simplification is supported by NMR data from the same cell culture, which show that the labeling of the fructosyl and glucosyl moieties of Suc is identical (Masakapalli et al., 2010). Statistical analysis of preliminary flux solutions also indicated that fluxes through NAD malic enzyme (all treatments) and NADP malic enzyme (hyperosmotic treatment) were determined with very low precision; thus, these fluxes were removed from the model for subsequent analyses. Previous work suggests that fluxes through these reactions are likely to be low in Arabidopsis cell suspensions (Williams et al., 2008). The complete model (in 13C-FLUX format) is given in Supplemental Table S2. Fitted fluxes were statistically analyzed to demonstrate that the labeling data contained sufficient information to reliably constrain each flux. All flux solutions passed the χ^2 test and are listed in Supplemental Table S3.

Comparison of Fluxes Predicted from the Genome-Scale Model and Estimated by ^{13}C-MFA

The metabolic models used in the genome-scale model and for ^{13}C-MFA are not identical. Details of how they were aligned are given in Supplemental

Table II. *Soluble metabolite abundances in Arabidopsis cell suspension cultures grown under control conditions (21°C, no mannitol), at high temperature (29°C), and under hyperosmotic stress (171 mM mannitol)*

Soluble metabolites were extracted with perchloric acid, and abundances were determined using ^{13}C-decoupled ^{1}H NMR spectroscopy. All values are in μmol mg^{-1} dry weight and are means ± SD from four replicates. Values indicated in boldface are significantly different (Student's t test, $P < 0.05$) from the corresponding value for control cells.

Metabolite	Treatment		
	Control	29°C	Hyperosmotic
Suc	0.060 ± 0.019	**0.098 ± 0.004**	0.086 ± 0.007
Citrate	0.112 ± 0.019	**0.252 ± 0.015**	**0.050 ± 0.012**
Malate	0.183 ± 0.019	0.211 ± 0.019	**0.059 ± 0.025**
Succinate	0.028 ± 0.029	0.011 ± 0.002	0.013 ± 0.003
Fumarate	0.002 ± 0.001	**0.000 ± 0.000**	**0.000 ± 0.000**
Asp	0.040 ± 0.008	**0.080 ± 0.003**	**0.013 ± 0.005**
Glu	0.135 ± 0.007	0.135 ± 0.008	**0.041 ± 0.005**
Gln	0.148 ± 0.027	**0.205 ± 0.009**	**0.039 ± 0.015**
γ-Aminobutyrate	0.041 ± 0.006	**0.071 ± 0.002**	**0.031 ± 0.004**
Ala	0.194 ± 0.077	**0.334 ± 0.039**	**0.042 ± 0.010**

Figure 1. Metabolic model used for ^{13}C-MFA. Free net fluxes are indicated in gray. For the control, elevated-temperature treatment, *chex2*, *ana1*, and *chex3* were free. For the mannitol treatment, where NADP malic enzyme was omitted, *chex2* and *tca1* were free. Free exchange fluxes for all models are indicated with circles. All other exchange fluxes were constrained to zero during parameter fitting. The arrows indicate the direction of positive flux as defined in the model. Flux names are given in italics. cit, Citrate; fum, fumarate; GABA, γ-aminobutyrate; αKG, α-ketoglutarate; OAA, oxaloacetate; PPP, pentose phosphate pathway. Standard abbreviations of amino acid names are used. Dashed boxes indicate where the subcellular localization of a metabolite or reaction cannot be inferred from the data or from the literature. The letters "p", "c," and "m" preceding metabolite names indicate separate pools of that metabolite in the plastid, cytosol, and mitochondrion, respectively. Output of CO_2 from the system is included in the model but not illustrated here. [See online article for color version of this figure.]

Table S4. It was possible to align 51 reactions in central carbon metabolism. A very good correlation was found between the flux values predicted by the genome-scale model and those estimated by ^{13}C-MFA (Fig. 2; $r^2 = 0.86$, $P < 0.001$). However, the significance of this result is reduced, because the fluxes for the reactions involved in the synthesis of biomass components (Tables I and II) are constrained to the same values in both approaches. Omitting these steps leaves 24 reactions representing the core of central carbon

metabolism: essentially glycolysis, the tricarboxylic acid (TCA) cycle, and the oxidative pentose phosphate pathway. These reactions can be legitimately compared, because their rates are estimated by independent means in the two approaches, and a good correlation was found ($r^2 = 0.77$, $P < 0.001$). To examine the flux correlation in more detail, the fluxes for each reaction were plotted against a metabolic network schematic (Fig. 3). It can be seen that for the majority of the reactions, the genome-scale model
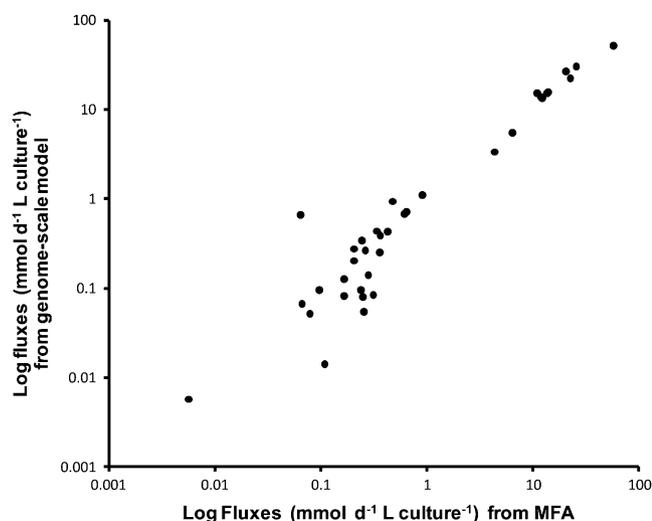
Figure 2. Comparison of fluxes in heterotrophic Arabidopsis cells determined by MFA and predicted from a genome-scale metabolic model. Cell culture growth rate and Glc consumption were measured between days 4 and 6 of the culture cycle, and biomass composition was determined at day 5. These data were used to constrain the flux solution within a genome-scale metabolic model. A parallel batch of cells was grown on [1-^{13}C]Glc, and the redistribution of label at day 5 was used to estimate fluxes by MFA.

predicts flux values that are a close match for those estimated by MFA. The exception to this is the oxidative pentose phosphate pathway, which carries a negligible flux in the genome-scale model. The oxidative reactions (reactions 1 and 2 in Fig. 3) carry zero flux in the genome-scale model solution in comparison with 14.2 mmol d^{-1} L^{-1} culture for the ^{13}C-MFA solution. The reversible nonoxidative reactions (reactions 5–7 in Fig. 3) have values of −0.35, −0.45, and −0.35 mmol d^{-1} L^{-1} culture in the genome-scale model and 7.0, 6.9, and 4.8 mmol d^{-1} L^{-1} culture in the ^{13}C-MFA solutions, respectively. The genome-scale model predicts fluxes in the TCA cycle accurately (to within 15%) but slightly overestimates the flux of glycolytic reactions (by an average of 30%).

A closer examination of the predicted fluxes for the reactions of glycolysis also reveals that the genome-scale model generates a network that is slightly different from that used for ^{13}C-MFA (Fig. 1). The reactions between glyceraldehyde 3-phosphate and phospho*enol*pyruvate (PEP; reactions 10–13 in Fig. 3) are combined into a single reaction "cphex" in the ^{13}C-MFA network. Because there are no branch points between these metabolites in the ^{13}C-MFA network, then by definition, at steady state they have the same flux: 25.6 mmol d^{-1} L^{-1} culture in the control cells. The fluxes predicted from analysis of the genome-scale model for the corresponding reactions 10 to 13 are 30.04, 30.04, 30.48, and 30.48 mmol d^{-1} L^{-1} culture, respectively. The fact that the fluxes for reactions 12 and 13 are slightly higher than those for reactions 10 and 11 means that there must be a branch point in this part

of the network that is not included in the ^{13}C-MFA model. This takes the form of a minor input flux into the 3-phosphoglyceric acid pool from Rubisco oxygenase activity, which is operating to support Gly and Ser biosynthesis (Poolman et al., 2009).

Prediction of Fluxes in Arabidopsis Cells Grown under Stress Conditions

To examine how well the genome-scale model is able to predict altered flux states, the Arabidopsis cells were cultured under different conditions and the flux predictions from the model were compared with the flux estimates obtained by ^{13}C-MFA. Two stress conditions were chosen, both of which are important from an agricultural perspective. First, growth temperature was increased from the control 21°C to 29°C. This increase in temperature is known to alter both the biomass composition and flux distribution in developing soybean (*Glycine max*) cotyledons (Iyer et al., 2008). Second, cells were cultured under hyperosmotic conditions generated by the addition of 171 mM mannitol. This treatment is known to induce gene expression patterns typical of abiotic stress (Clifton et al., 2005) and is likely to trigger a metabolic response (Skirycz et al., 2010). It was found that both of these treatments led to a significant change in growth rate, substrate utilization, and biomass composition (Tables I and II). The growth of the cells was significantly slower: the rate of biomass production under increased temperature and hyperosmotic stress was 33% and 39% of the control, respectively. Both treatments also caused a significant decrease in Glc consumption rate, although this was much more pronounced under hyperosmotic stress, in which Glc consumption was only 40% of the control, compared with 82% for increased temperature. Both treatments also led to a pronounced shift in the biomass composition (Table I). Considering the changes in biomass composition, growth rate, and Glc consumption rate together, the altered demands on the carbon assimilated can be calculated. Under hyperosmotic stress, a greater proportion of Glc consumed was used for cell wall (30% of Glc consumed compared with 25% for the control) and for protein (15% of Glc consumed compared with 11% for the control). Under heat treatment, the proportion of Glc consumed that was converted into biomass was substantially reduced: biomass represented only 23% of the Glc consumed in comparison with 57% for the control. Of the biomass produced, there was proportionally less cell wall and protein (approximately 20% less of each). There were also pronounced shifts in soluble metabolite abundances, with a general decrease in nearly all metabolites in the mannitol treatment and increases in amino acids, citrate, and Suc at the higher temperature (Table II).

MFA revealed the impact that these changes had on the flux distribution. It was found that increased temperature caused a substantial, approximately 2-fold, increase in TCA cycle fluxes (Fig. 4A; Supplemental
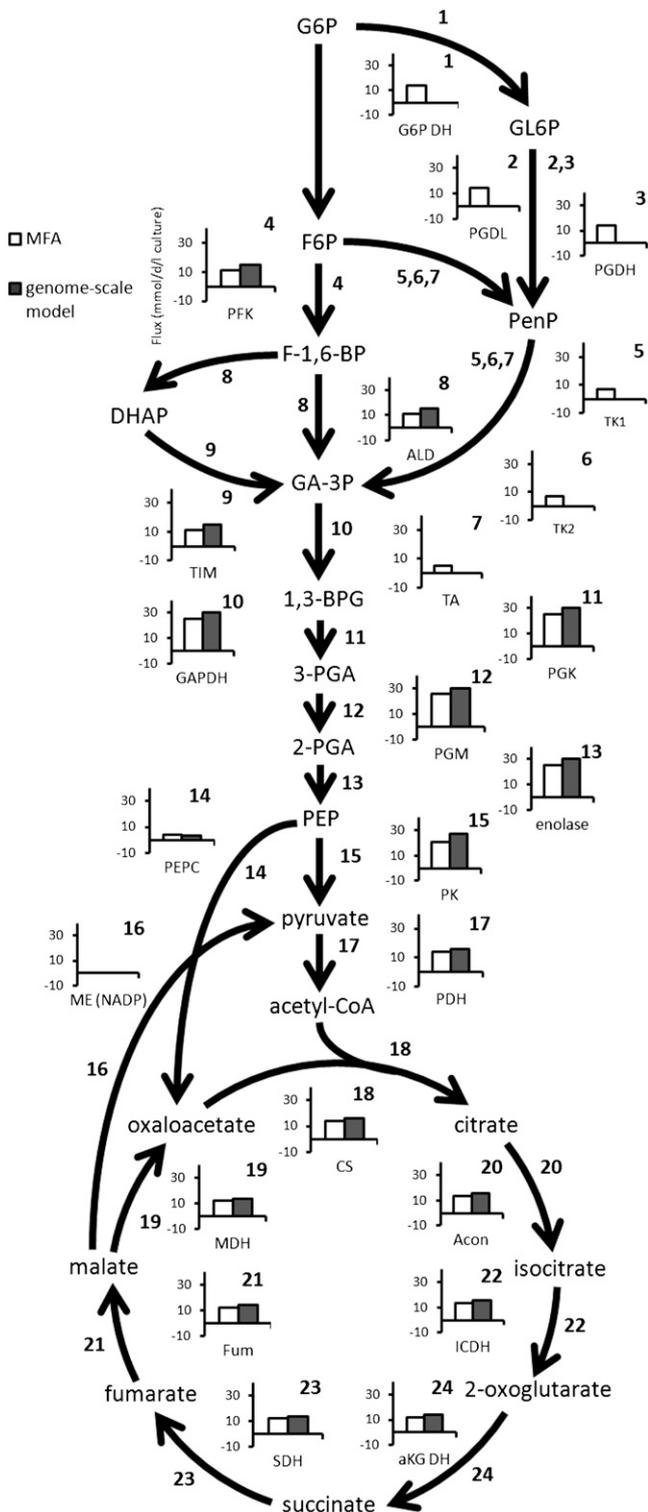
G6P

1

1
30
10
-10
G6P DH

GL6P

2,3

2
30
10
-10
PGDL

3
30
10
-10
PGDH

☐ MFA

■ genome-scale
model

Flux (mmol/d/l culture)

4
30
10
-10
PFK

F6P

4

5,6,7

PenP

F-1,6-BP

5,6,7

5
30
10
-10
TK1

8

DHAP

8
30
10
-10
ALD

6
30
10
-10
TK2

9

GA-3P

9
30
10
-10
TIM

10

7
30
10
-10
TA

10
30
10
-10
GAPDH

1,3-BPG

11

3-PGA

11
30
10
-10
PGK

12
30
10
-10
PGM

2-PGA

12

13

14
30
10
-10
PEPC

PEP

13
30
10
-10
enolase

15
30
10
-10
PK

14

pyruvate

15

16
30
10
-10
ME (NADP)

17
30
10
-10
PDH

acetyl-CoA

17

18

16

oxaloacetate

18
30
10
-10
CS

citrate

20

19
30
10
-10
MDH

20
30
10
-10
Acon

19

malate

isocitrate

21
30
10
-10
Fum

22
30
10
-10
ICDH

22

21

fumarate

23
30
10
-10
SDH

24
30
10
-10
aKG DH

24 2-oxoglutarate

23

succinate

Figure 3. Comparison of fluxes of central carbon metabolism determined by MFA and predicted from a genome-scale metabolic model. The metabolic diagram shows the reactions of glycolysis, the oxidative pentose phosphate pathway, and the TCA cycle. Each reaction is numbered, cross-referencing Table I, and each bar graph showing flux values (in mmol d^{-1} L^{-1} cell culture) is labeled with the corresponding reaction number. Metabolites are as follows: G6P, Glc 6-P; F6P, Fru 6-P; GL6P, gluconate 6-phosphate; PenP, pentose phosphate; F-1,6-BP, Fru

Table S3). Fluxes in glycolysis and the oxidative pentose phosphate pathway were not significantly affected, but there was a significant decrease in the PEP carboxylase reaction flux. In contrast, the mannitol treatment had no effect on the relative flux distribution but instead led to a coordinated decrease of fluxes through glycolysis, the oxidative pentose phosphate pathway, and the TCA cycle (Fig. 4B; Supplemental Table S3). Fluxes predicted from the genome-scale model accurately reflected both of these very different flux scenarios, correctly identifying a 2-fold increase in TCA cycle flux and an approximately 70% decrease in the PEP carboxylase reaction flux at higher temperature and a coordinated decrease of all fluxes to 30% to 35% of control values under hyperosmotic stress (Fig. 4). The only exception was the oxidative pentose phosphate pathway, which, as under control conditions, was poorly predicted under the two stress conditions.

Mitochondrial Respiration in Cells Grown at High Temperature

The increased TCA cycle flux at high temperature is accompanied by an equivalent increase in mitochondrial electron transport: flux through the mitochondrial electron transport chain complexes is predicted by the genome-scale model to increase by an average of 1.9-fold under increased temperature (Supplemental Table S1). To investigate the bioenergetic status of mitochondria in vivo in response to increased temperature, Arabidopsis cells were incubated with a fluorescent probe, tetramethyl rhodamine methyl ester (TMRM), which accumulates in mitochondria according to membrane potential. An appreciable reduction in TMRM signal was observed in cells cultured at increased temperature (Fig. 5, B and D). To quantify the TMRM signal, the cells were counterstained with the vital stain fluorescein diacetate (FDA) as a reference (controlling for the number of cells in the image and general variations in dye uptake). A total of 15 images from three independent cell suspensions for each condition were analyzed. The average TMRM fluorescence signal relative to the FDA signal decreased by 31% in the high-temperature cells in comparison with control cells.

1,6-bisP; 3-PGA, 3 phosphoglyceric acid; 2-PGA, 2 phosphoglyceric acid. Enzymes are as follows: (1) G6P DH, Glc 6-P dehydrogenase; (2) PGDL, 6-phosphogluconolactonase; (3) PGDH, 6-phosphogluconate dehydrogenase; (4) PFK, phosphofructokinase; (5) TK1, transketolase 1; (6) TK2, transketolase 2; (7) TA, transaldolase; (8) ALD, aldolase; (9) TIM, triosphosphate isomerase; (10) GAPDH, glyceraldehyde 3-phosphate dehydrogenase; (11) PGK, phosphoglycerate kinase; (12) PGM, phosphoglyceromutase; (13) enolase; (14) PEPC, phospho-*enol*pyruvate carboxylase; (15) PK, pyruvate kinase; (16) ME (NADP), NADP-dependent malic enzyme; (17) PDH, pyruvate dehydrogenase; (18) CS, citrate synthase; (19) MDH, malate dehydrogenase; (20) Acon, aconitase; (21) Fum, fumarase; (22) ICDH, isocitrate dehydrogenase; (23) SDH, succinate dehydrogenase; (24) αKGDH, α-ketoglutarate dehydrogenase.
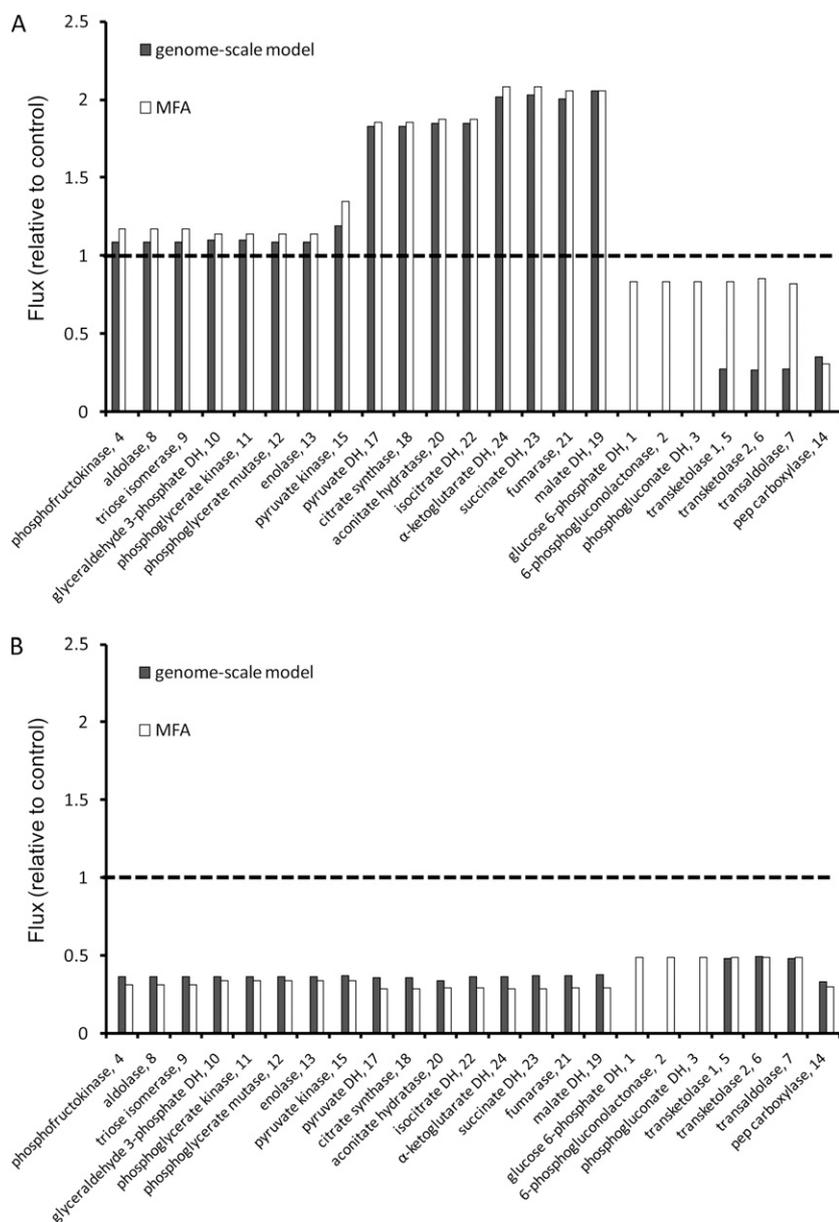
Figure 4. Comparison of fluxes in Arabidopsis cell suspensions grown for 5 d under control conditions, high temperature (29°C; A), and hyperosmotic stress (B). Fluxes were determined by MFA and predicted from a genome-scale model, and each graph shows the flux for the indicated reactions relative to the value for the control (indicated by the dashed line). Reaction 16 (NADP-malic enzyme) is not shown because it carries no flux in the genome-scale model solutions and was omitted from the ^{13}C-MFA model for the mannitol treatment.

DISCUSSION

Constraints-Based Metabolic Modeling Can Accurately Predict Fluxes in Central Carbon Metabolism

Using the independently constrained ^{13}C-MFA flux estimates, it was possible to assess how well constraints-based genome-scale modeling is able to predict fluxes in the three main pathways of heterotrophic carbon metabolism: glycolysis, the TCA cycle, and the oxidative pentose phosphate pathway. For glycolysis and the TCA cycle, there was good agreement, with the genome-scale model able to predict flux values similar to ^{13}C-MFA. The genome-scale model was also able to predict specific flux changes in cells cultured at high temperature (increased TCA cycle and decreased PEP carboxylase fluxes) and a general decrease in fluxes

under mannitol treatment. Two lines of evidence demonstrate that the good match between the predicted fluxes and those from ^{13}C-MFA is not merely due to structural constraints within the model when certain rates and compositions of biomass production are specified. First, use of different objective functions in a genome-scale model of *Escherichia coli* resulted in significantly different fluxes through glycolysis, the TCA cycle, and the oxidative pentose phosphate pathway (Schuetz et al., 2007). Second, the flux solution for the Arabidopsis genome-scale model without the generic ATPase reaction to account for cell maintenance ATP demands is substantially different both in quantitative terms and in the reactions operating (Poolman et al., 2009). In both of these cases, fluxes in central carbon metabolism vary even though the rate and
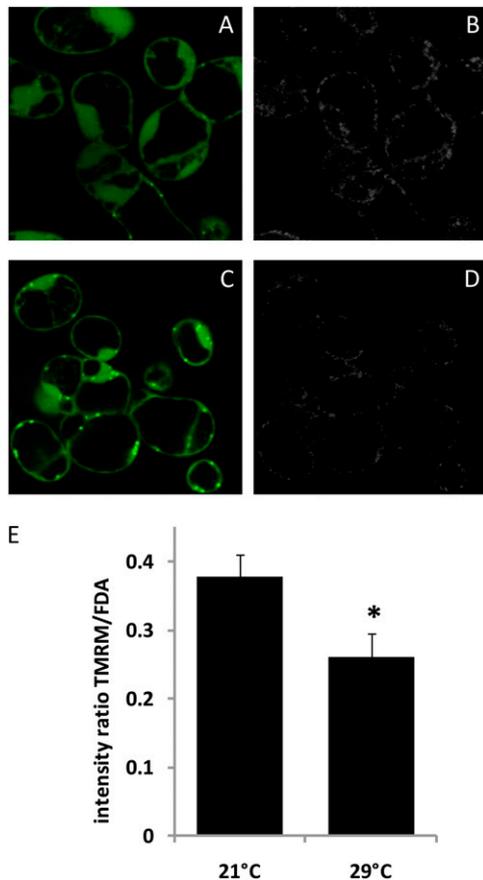
Figure 5. Staining of mitochondria with TMRM as a qualitative indicator of mitochondrial membrane potential. A to D, Control cells grown at 21°C (A and B) and cells grown at 29°C (C and D) were stained with TMRM (B and D) and counterstained with FDA (A and C). Representative confocal laser scanning microscopy images are shown. E, Three independent cell cultures were analyzed, and the TMRM/FDA signal ratio was calculated for each image. Values are means ± SE. The asterisk indicates significantly different from control (Student's *t* test, $P < 0.05$). [See online article for color version of this figure.]

proportion of biomass synthesis are fixed, demonstrating that fluxes in central carbon metabolism are not rigidly constrained to biomass synthesis fluxes.

The genome-scale model did not predict realistic fluxes for the oxidative pentose phosphate pathway. The oxidative reactions carried no flux in any of the predicted flux solutions, and flux through the reversible nonoxidative reactions was 14-fold lower under control conditions than MFA estimates. Given the importance of the oxidative pentose phosphate pathway in the provision of NADPH, particularly for nitrate assimilation and fatty acid biosynthesis, the question arises of the source of NADPH in the genome-scale model. Inspection of the flux solution revealed that the major source of NADPH was NADP-dependent glyceraldehyde 3-phosphate dehydrogenase (GAPDH). In terms of the objective function of the model (minimization of overall fluxes), this makes sense: not only does the GAPDH route to

NADPH require fewer reactions than the oxidative pentose phosphate pathway (and hence a lower sum of fluxes), but the concomitant carbon flux (production of dihydroxyacetone phosphate) is simply incorporated into glycolysis. Presumably, thermodynamic or enzyme activity limitations prevent NADP-dependent GAPDH from fulfilling this role in vivo.

Altered Demand for Specific Biomass Precursors Has Little Impact on Central Carbon Metabolism Fluxes in Arabidopsis Cell Suspension Cultures

Synthesis of the main components of biomass (cell wall, protein, lipid, and starch) requires precursors, reductant, and ATP generated in the pathways of central carbon metabolism. Precursors for the different biomass components are drawn from different points in central carbon metabolism, and there are widely differing energy and reductant requirements (Schwender, 2008). For example, synthesis of protein requires the most ATP per mass unit synthesized, and synthesis of lipid requires three times as much NADPH as for protein. Synthesis of starch and cell wall carbohydrate requires no reductant and approximately 8-fold less ATP than an equivalent mass of protein. Thus, changes in the rate of synthesis of different biomass components might be reflected in altered fluxes in central carbon metabolism.

Under hyperosmotic stress, biomass accumulation decreased substantially, so the observed general decrease in fluxes is to be expected. However, the proportion of different biomass components synthesized was altered, with significant increases in the proportion of consumed Glc committed to cell wall and protein. The latter, in particular, would impose an increase in the ATP demand on the system as well as requiring increased withdrawal of precursor metabolites at a number of points in glycolysis and the TCA cycle. However, this was achieved with no significant changes in the relative fluxes through these pathways. This can be explained if the biosynthetic processes supporting cell growth account for only a small fraction of the total ATP demand in the cell and therefore impose only a minor constraint on TCA cycle flux. In fact, this is likely. MFA demonstrates that fluxes through the central carbon network in heterotrophic Arabidopsis cells can support seven times the rate of ATP synthesis required for biomass synthesis (Masakapalli et al., 2010). Similarly, genome-scale modeling only accommodates the observed Glc consumption rate if 80% of the total ATP produced is used for purposes other than biomass component synthesis (Poolman et al., 2009). These other costs include turnover and resynthesis of polymers, especially protein, substrate uptake, subcellular metabolite transport, and maintenance of membrane energization. Similar conclusions have been reached with other systems. For example, in developing sunflower (*Helianthus annuus*) seeds, only 11% of the ATP produced was used for biomass production and polymerization (Alonso et al., 2007).

Further work is required to establish more precisely how the cellular ATP budget is allocated (Piques et al., 2009), but it seems likely that cell maintenance ATP costs exert a much greater constraint on the ATP-producing pathways (glycolysis and the TCA cycle) than synthesis of biomass components. This emphasizes the importance of incorporating the major energy-consuming processes into models of metabolism. In the genome-scale model presented here, cell maintenance ATP costs are simulated indirectly by varying a generic ATPase reaction until the rate of consumption of Glc matched that observed experimentally. The ability of the model to accurately predict glycolytic and TCA cycle fluxes suggest that this indirect method produces a reasonable estimation of actual ATP synthesis rates and is certainly less problematic than trying to estimate polymer turnover rates and other cell maintenance costs (Nielsen et al., 2003). The approach does lead to a slight overestimation of glycolytic flux, but this would undoubtedly improve with the introduction of parameters to constrain the oxidative pentose phosphate pathway flux more effectively.

Rate of Synthesis of Soluble Metabolites May Balance Central Carbon Network Fluxes

While the relative flux distribution of central carbon metabolism was stable under hyperosmotic stress, the rates of synthesis of soluble metabolites were significantly different, with decreases in the majority of measured metabolites per unit dry weight. This is consistent with recent metabolomic observations of Arabidopsis leaves under osmotic stress (Skirycz et al., 2010). Inspection of the flux distribution suggests that decreases in relative fluxes to soluble metabolites may help to offset the relative increased demand for precursors for protein and cell wall biosynthesis, leaving the overall flux distribution unchanged. For example, when fluxes are considered relative to the same rate of biomass production, withdrawal of carbon from the TCA cycle is actually lower under hyperosmotic stress (0.70 arbitrary units carbon d^{-1} flask^{-1}) than in control cultures (0.83 arbitrary units carbon d^{-1} flask^{-1}), despite the increased demand for precursors for protein synthesis. In effect, the synthesis of soluble metabolites is varied to buffer changing demands for precursors for biomass polymer synthesis, such that the flux through the central carbon pathways is able to remain constant. This contrasts with variations in the high-flux backbone in *E. coli* observed when constraints-based modeling was used to examine the effect of altered growth conditions (Almaas et al., 2004). However, the altered growth conditions in that study consisted of changing the carbon substrate in the growth medium, which would inevitably impinge on the flux modes in the central network. Similarly, in plant metabolism, a switch between inorganic and organic nitrogen sources causes substantial changes in the flux distribution in the central metabolic network (Junker et al., 2007). In contrast, the analysis here

suggests that when the substrate source is the same, which is the normal situation for plant cells, then the relative flux distribution in the central metabolic network is largely insensitive to abiotic stress conditions.

Increased Growth Temperature Leads to a Considerable Decrease in Carbon-Use Efficiency

Carbon-use efficiency can be calculated from the Glc consumption rate and the fluxes through the CO_2-evolving reactions estimated by MFA or predicted by analysis of the genome-scale model. Carbon-use efficiency was 58% ± 5% and 64% ± 9% for control and hyperosmotic stress, respectively, values that were comparable to previous estimates for the Arabidopsis cell suspension culture (Williams et al., 2008; Masakapalli et al., 2010), but only 21% ± 4% in cells cultured at elevated temperature. Effectively, per unit of carbon incorporated into biomass, 2-fold more carbon was lost as CO_2 under increased temperature in comparison with the control. The MFA analysis suggests that all of this additional CO_2 is released by the TCA cycle, as opposed to other decarboxylating reactions such as the oxidative steps of the oxidative pentose phosphate pathway. CO_2 release from fatty acid synthesis decreased in line with the decreased growth rate.

There is much interest in the response of respiration to temperature because it has substantial relevance to the global carbon cycle and climate change. It has been widely observed that increased temperature leads to short-term increases in respiration (Atkin and Tjoelker, 2003). However, because these observations are based on total CO_2 release or oxygen uptake, it is not clear whether processes other than respiration contribute to the altered CO_2 release. From the data presented here, it is clear that respiration alone is responsible for the increased CO_2 release. Under control conditions, the MFA-derived flux map reveals that 60% of the CO_2 released was from respiration, 27% from the oxidative pentose phosphate pathway, and 9% from fatty acid synthesis. At high temperature, 82% of the total CO_2 released was from respiration. The response of plant respiration to temperature is known to be acclimative, with acclimation occurring within 1 to 2 d of growth at the elevated temperature (Covey-Crump et al., 2002). Acclimation is not apparent after 6 d of growth of the cell suspension culture, which is consistent with acclimation involving tissue-level morphological and cellular changes (Armstrong et al., 2006) that are unlikely to be replicated in a cell culture.

The underlying mechanism for the effect of temperature on respiration is unknown. The fact that other fluxes are not similarly responsive rules out a simple temperature effect on enzyme kinetics. Two other explanations for the increase in the TCA cycle flux can be put forward. The first is that there may have been an increase in the demand for ATP. If so, this ATP demand must be in the cell maintenance fluxes, because the changes in biomass composition when grown at high temperature (decreased protein and

starch) would actually require less ATP. Alternatively, it is possible that the coupling of the mitochondrial electron transport chain to ATP synthesis is reduced. The reduction in TMRM signal (Fig. 5), indicating partial depolarization of mitochondria, is consistent with either of these scenarios. If ATP demand is higher, then an increased rate of ATP synthesis would lead to greater dissipation of the mitochondrial inner membrane proton gradient (Brown et al., 1990). If partial uncoupling is occurring, the mitochondrial proton gradient would also be reduced via several potential mechanisms. First, increased temperature increases leakage of protons across the mitochondrial membrane (Chamberlin, 2004) due to changes in membrane fluidity and structure (Brand et al., 2003). However, proton leak only accounts for 20% of the respiration rate on average (Rolfe and Brand, 1997), so this is unlikely to explain the doubling in respiration observed here. Alternatively, the activity of nonphosphorylating bypasses such as alternative oxidase, alternative NAD(P)H dehydrogenases, or uncoupling protein may increase. However, the activities of the alternative oxidase and the uncoupling protein are generally associated with a decrease, not an increase, in temperature (Gonzalez-Meler et al., 1999; Nantes et al., 1999). Further work is clearly required to establish the cause of the increased respiratory rate.

Hyperosmotic Stress Leads to a Coordinated Decrease in Flux through Central Carbon Metabolism

The hyperosmotic growth condition used here mimics the effect of drought, causing water loss in the treated cells. Drought stress is known to cause a reduction in plant growth (Boyer, 1982). While this is mainly due to reduced photosynthetic activity, mitochondrial respiration is also thought to be a critical component of the response (Atkin and Macherel, 2009; Skirycz et al., 2010). Generally, respiration is observed to decrease during osmotic stress (Galle et al., 2010), although there is considerable variability in the response (Atkin and Macherel, 2009). Using MFA, it was possible to establish that, as well as a decrease in respiratory CO_2 release from the TCA cycle, there was also a general decrease in the other pathways of central carbon metabolism. This is a significant observation because it suggests that the decrease of mitochondrial metabolic activity may be part of a wider and coordinated metabolic response that goes beyond a mitochondria-specific effect. One possibility is that carbon is diverted from glycolysis/TCA cycle/oxidative pentose phosphate pathway to be used for the synthesis of carbohydrate reserves (Seki et al., 2007). However, although there was an increase in cell wall synthesis in the Arabidopsis cell culture in relative terms, the rate of cell wall synthesis was approximately 2-fold lower in absolute terms. An alternative possibility is that the stress condition inhibits the uptake of substrate (Glc) into the cells. This is unlikely to explain the observed inhibition of leaf respiration, but it could be a factor in

heterotrophic tissues or in young sink leaves. In this context, it is relevant that induction of genes of the "mitochondrial dysfunction regulon" occurs only in young, rapidly growing leaves and not in mature source leaves (Skirycz et al., 2010). Clearly, any conclusion drawn from analysis of a cell-suspension culture would need to be verified in whole plant tissues, but MFA and metabolic modeling can reveal aspects of the metabolic response that are not necessarily apparent using other approaches. For, example, an induction of glycolytic and TCA cycle proteins in response to osmotic stress in Arabidopsis cell suspension cultures (Ndimba et al., 2005) might lead one to the conclusion that flux in these pathways is increased, whereas the flux analysis demonstrates the opposite.

CONCLUSION

This work demonstrates that it is possible to predict fluxes accurately in central carbon metabolism in heterotrophic Arabidopsis cells using an objective function based on flux minimization. The predictions are not only accurate in absolute terms but also in predicting the direction and magnitude of the changes caused by altered growth conditions. However, further work is required to improve the prediction of fluxes in the oxidative pentose phosphate pathway, perhaps through the use of alternative objective functions. It would also be desirable to include a more complete description of the subcellular compartmentation of central carbon metabolism than the one used here, although parallel reactions in different compartments present challenges for both constraints-based modeling (de Oliveira Dal'Molin et al., 2010) and ^{13}C-MFA (Masakapalli et al., 2010). Overall, the work presented here raises the possibility that constraints-based modeling may be useful as a high-throughput method for predicting net fluxes through the central metabolic network in a range of plant tissues and genotypes. This would allow constraints-based analysis to be used as a rapid precursor to detailed analysis of forward and reverse fluxes at subcellular resolution using ^{13}C-MFA. The work also reveals new insights into the metabolic response of cells to altered environment, demonstrating specific changes in the TCA cycle and PEP carboxylase flux to increased temperature and a general decrease in flux through central carbon metabolism during osmotic stress.

MATERIALS AND METHODS

Chemicals

Chemicals were purchased from Sigma-Aldrich unless otherwise stated.

Arabidopsis Cell Suspension Culture

Heterotrophic cell suspensions (May and Leaver, 1993) of Arabidopsis (*Arabidopsis thaliana*) were grown in 250-mL Erlenmeyer flasks and harvested as before (Williams et al., 2008). For increased temperature treatment, cell

suspensions were incubated at 29°C (control, 21°C). For hyperosmotic treatment, mannitol was added to the growth medium to a final concentration of 171 mM. For measurements of growth rate and Glc consumption, and for labeling to isotopic steady state, cell cultures were grown in 100-mL flasks and the volumes of growth medium and inoculum were reduced proportionally. Growth rate and Glc consumption measurements were made by removing 2-mL samples daily from three to four cultures. Culture samples were briefly centrifuged, a sample of supernatant was removed for analysis of Glc abundance, and the mass of the cell pellet was determined after lyophilization. The rate of biomass increase was calculated from the change in mass within cultures between 4 and 6 d after subculture. Glc concentration was determined using a standard enzymatic assay (Sweetlove et al., 1996), and rate of consumption was calculated from the change in concentration within cultures between 4 and 6 d after subculture, allowing for the change in volume of the medium resulting from culture growth.

Labeling to Isotopic Steady State

Cell suspensions (four replicates per treatment) were labeled to isotopic steady state by subculturing into cell culture medium where 25% (molar) of Glc had been replaced with [1-^{13}C]Glc (99 atom %; Cambridge Isotopes) and were harvested after 5 d of growth. Previous work showed that cells grown under control conditions reached isotopic steady state after 5 d of growth (Williams et al., 2008), and isotopic steady state is likely to have been achieved for all the treatments described here. This was tested by comparing the incorporation of ^{13}C into fragments anticipated to have the same metabolic origin (e.g. Asp and Asn, fragment C2-C4). This analysis did not reveal any major differences in labeling (data not shown), indicating that soluble metabolites reached isotopic steady state after 5 d of growth.

In contrast, comparison of labeling between amino acids in soluble metabolite extracts and those derived from hydrolyzed protein revealed consistently higher levels of ^{13}C incorporation into amino acids from soluble extracts (Supplemental Table S2). This suggests the presence of pools of protein that turn over slowly and thus remain unlabeled. In support of this interpretation, analysis using one-dimensional ^{13}C NMR, which is insensitive to unlabeled compounds, showed that the label distribution within amino acids hydrolyzed from protein did reach isotopic steady state (Williams et al., 2008). Accordingly, the metabolic model used to analyze the labeling data here includes modifications, similar to those reported by Lonien and Schwender (2009), allowing the abundance of unlabeled protein, and hence its influence on amino acid labeling, to be determined during parameter fitting, based on the assumption that extracted protein is composed of a mixture of protein labeled to isotopic steady state and unlabeled protein.

Extraction and Fractionation of Labeled Metabolites and Biomass Components

Soluble metabolites were extracted from 30 mg of lyophilized cell-suspension cultures using perchloric acid (Kruger et al., 2008) and redissolved in 5 mL of 5 mM KH$_2$PO$_4$, pH 5.0, after the final drying step. Prior to GC-MS analysis, extracts were fractionated into neutral, acidic, and basic components using anion- and cation-exchange chromatography. Protein was extracted from the pellet remaining from perchloric acid extractions using a solution of 6 M urea and 2 M thiourea. Protein was prepared for hydrolysis by precipitation with 15% (v/v) ice-cold trichloroacetic acid and repeated washing with acetone and then hydrolyzed by heating to 100°C for 24 h in 6 M HCl at atmospheric pressure. Liberated amino acids were purified using cation-exchange chromatography. Starch was enzymatically digested from pellets remaining after extraction of soluble metabolites and protein (Allen et al., 2007).

Biomass Composition Analysis

Analysis of biomass composition in lyophilized cell suspension culture was carried out as before (Williams et al., 2008).

NMR Spectroscopy

Unfractionated perchloric acid extracts were prepared for NMR spectroscopy by mixing 200 μL of extract with 700 μL of D$_2$O (Apollo Scientific) containing 2 mM EDTA and 1 mM 3-(trimethylsilyl)-[2,2,3,3-^{2}H$_4$]propionic acid. One-dimensional ^{1}H NMR spectra of perchloric acid extracts were recorded at 20°C on a Varian Unity Inova 600 spectrometer using a 5-mm HCN triple-resonance z-gradient probe and the standard Varian pulse program with a relaxation delay of 2 s, including a 1.98-s presaturation pulse to suppress the water signal, a 90° pulse angle, a spectral width of 10 ppm, and a 4-s acquisition time. For ^{13}C-labeled samples, ^{13}C-broadband decoupling (WURST-40) was applied during the detection period to remove ^{1}H-^{13}C coupling, the acquisition time was reduced to 2 s, and the delay before the presaturation pulse was increased to 4 s to eliminate sample heating. Spectra were processed and analyzed using NUTS (Acorn NMR). One-dimensional ^{1}H free induction decays were zero filled and baseline corrected. Line broadening (exponential multiplication) was applied at 0.5 Hz. After Fourier transformation, manual phase correction was applied and linear regression was used to flatten the spectral baseline prior to quantification. Spectra were referenced to 3-(trimethylsilyl)-[2,2,3,3-^{2}H$_4$]propionic acid at 0 ppm. ^{1}H assignments were based on literature values, comparison with pure standards, and the results of two-dimensional NMR experiments (data not shown). Positional enrichments of Ala were measured using line fitting of coupled spectra and are assigned an accuracy of 2% (fractional enrichment scale).

GC-MS Analysis

Sample Preparation

Samples, typical volume 10 to 100 μL depending on the extent of labeling, were dried using a Speed-Vac system prior to derivatization. For samples containing amino acids and organic acids, 43 μL of pyridine was added to each tube, and samples were shaken at 37°C for 1 h and then briefly centrifuged to collect any condensation. A total of 60 μL of 2,2,2-trifluoro-*N*-methyl-*N*-trimethylsilyl-acetamide (HiChrom) was added to each tube, and samples were shaken at 37°C for 30 min. Samples were centrifuged for 10 min at 16,000g to pellet any insoluble material, and the supernatant was transferred to 8-mm glass vials (Chromacol). For sugar-containing samples, 50 μL of 20 mg mL^{-1} methoxyamine hydrochloride in pyridine was added to each tube, and samples were shaken at 37°C for 2 h. A total of 70 μL of 2,2,2-trifluoro-*N*-methyl-*N*-trimethylsilyl-acetamide was used for the derivatization.

GC-MS

GC-MS analysis was carried out using an Agilent 7890A GC device coupled to an Agilent 5975C quadrupole mass spectrometer. For all methods, the carrier gas was helium and flow through the column was kept constant at 0.6 mL min^{-1}. The sample (1 or 2 μL) was injected in splitless mode at 230°C. All samples were run on either a Varian VF5-ms column (30 m, 10 m guard column, 0.25 μm i.d.) or an Agilent HP 5-ms column (30 m, 0.25 μm i.d.), each containing the equivalent of 5% phenyl and 95% diphenyl polysiloxane as a stationary phase. For sugar-containing samples, the oven temperature was initially held constant at 70°C for 5 min and then ramped up to 350°C at 5°C min^{-1}. The temperature was then decreased and held at 330°C for 5 min before being decreased to 70°C at 120°C min^{-1}. For amino acid and organic acid samples, the oven temperature was initially held constant at 70°C for 5 min and then ramped up to 280°C at 5°C min^{-1}, held there for 3 min, before being decreased to 70°C at 120°C min^{-1}. In the case of organic acid-containing samples, a solvent delay of 19 min was used to avoid detection of a large phosphate-trimethyl silyl peak.

For all samples, the MS source temperature was 250°C, the MS quadrupole temperature was 150°C, and the transfer line temperature was 250°C. The mass spectrometer was tuned to signals from perfluorotributylamine before each batch of samples. Depending on the sample type, the mass spectrometer was operated in scan or single ion monitoring mode. In scan mode, ions with masses between 50 and 600 atomic mass units were monitored at a rate of 2.66 scans s^{-1}. In single ion monitoring mode, ions corresponding to known fragments were monitored and the dwell time for each group of ions was adjusted from 10 to 30 ms depending on the number of ions in the group to ensure that peaks were properly defined.

Data Analysis

Baseline correction was carried out for all chromatograms acquired using scan mode using MetAlign (Lommen, 2009) with the following parameters: peak slope factor, 1× noise; peak threshold factor, 2× noise; average peak width at half height, five scans. Compound identification was performed using AMDIS32 (National Institute of Standards and Technology) and by

comparison against an extensive library of trimethyl silyl-derivatized plant metabolites (Kopka et al., 2005) using MSSearch (National Institute of Standards and Technology). Where identification of compounds by comparison of mass spectra was ambiguous, assignment of peaks was confirmed by spiking samples with a known amount of pure candidate compounds. Analysis of ^{13}C incorporation was carried out using Chemstation (MSD version; Agilent). To avoid problems associated with fractionation of heavy isotopes across the width of a GC-MS chromatographic peak (Allen and Ratcliffe, 2009), the mass spectra of chromatographic peaks were averaged before export of mass-to-charge ratio and ion count data to tab-delimited text files. To calculate fractional enrichments, averaged mass spectra were corrected for the presence of naturally occurring heavy isotopes using published software (Wahl et al., 2004). The identity and chemical formulae of fragments that are required to do this were taken from the literature (Laine and Sweeley, 1971; Leimer et al., 1977; Huege et al., 2007) or deduced from the fragmentation pattern of related molecules (Leimer et al., 1977).

In order to ensure that labeling measurements of appropriate quality for flux analysis were made (i.e. with both high accuracy and high precision; Antoniewicz et al., 2007), mass spectra were manually checked and fragments were excluded from further analysis if they exhibited large M-1 peaks or clearly overlapped with other fragments. MFA requires estimates of the accuracy of the mass isotopomer distribution measurements, and these were made on the basis of the accuracy of measurements of the same mass isotopomers in unlabeled metabolites or samples (Allen et al., 2009b). Where the mass isotopomer could be measured to within 1% of its predicted value at natural abundance ^{13}C, an error of 1% (fractional enrichment scale) was used. If the mass isotopomer abundance was accurate to between 1% and 2%, an error of 2% was applied, while if the accuracy was worse than 2%, the entire fragment was excluded from further analysis.

Metabolic Modeling

The genome-scale metabolic model was essentially the same as described before (Poolman et al., 2009) with the exception of a correction for the direction of the PEP carboxylase reaction (so that oxaloacetate is the reaction product) and the inclusion of a cytosolic malate dehydrogenase (MALATE-DH-RXN) in addition to the mitochondrial one (MalDH). Flux solutions were obtained using linear programming to minimize the sum of fluxes in a solution space constrained by biomass component synthesis rates and an ATPase reaction matched to the Glc consumption rate as before (Poolman et al., 2009).

^{13}C-MFA was carried out using 13C-FLUX (version 20050329; Wiechert et al., 2001) running within a Ubuntu Linux environment as described by Williams et al. (2008). GC-MS measurements were incorporated into the input. ftbl files as outlined by Wiechert et al. (2001). ^1H NMR measurements of positional enrichment were incorporated into the "Label Measurements" section of the.ftbl files. The 13C-FLUX implementation of the Donlp2 algorithm (Peter Spellucci, Technische Universität Darmstadt) was used for parameter fitting in Bootstrap Monte Carlo mode, in conjunction with a custom script (Masakapalli et al., 2010) to obtain over 100 feasible flux solutions for each treatment. The solutions with the 50 lowest residua were then averaged, and this average solution was used as a starting point for a final optimization without Monte Carlo labeling of the labeling data (Masakapalli et al., 2010). The EstimateStat component of 13C-FLUX was used to determine errors on these final flux estimates. Output fluxes were held constant during parameter optimization but were set as "free," and their values and errors were given in the model definition during EstimateStat analysis.

Confocal Microscopy

Cell-suspension cultures grown under different temperature regimes for 4 d were stained with 200 nM TMRM (made from a 100 mM stock in dimethylsulfoxide) for 15 min while maintaining their respective culture temperature. Cells were counterstained with 0.0005% FDA (made from a 0.5% [w/v] stock in dimethylsulfoxide) for 5 min. Cells were washed in supernatant of their respective culture flask and imaged immediately using a Zeiss confocal microscope (LSM510META) using excitation/emission at 543/545 to 615 nm (TMRM) and 488/500 to 530 nm (FDA). Images were collected with a 63× lens (Zeiss Plan-Apochromat 63×/1.4 Oil DIC). Cells were selected randomly in bright-field mode before imaging TMRM fluorescence. To ensure specific staining of TMRM to mitochondrial membrane potential, cells treated with 40 μM carbonyl cyanide 3-chlorophenylhydrazone were used as a negative control (data not shown). Background was subtracted in either channel, and only nonsaturated pixels with an intensity of 4 SD above

background were included in the analysis. The ratio between both channels was then calculated frame by frame.

Supplemental Data

The following materials are available in the online version of this article.

Supplemental Table S1. Metabolic fluxes in heterotrophic Arabidopsis cells predicted from a genome-scale model.

Supplemental Table S2. 13C-FLUX model of central metabolism in heterotrophic Arabidopsis cells and label measurements.

Supplemental Table S3. Metabolic fluxes in heterotrophic Arabidopsis cells determined by steady-state ^{13}C-MFA.

Supplemental Table S4. Alignment of the genome-scale and ^{13}C-MFA metabolic models.

LITERATURE CITED

Allen DK, Libourel IGL, Shachar-Hill Y (2009a) Metabolic flux analysis in plants: coping with complexity. Plant Cell Environ **32:** 1241–1257

Allen DK, Ohlrogge JB, Shachar-Hill Y (2009b) The role of light in soybean seed filling metabolism. Plant J **58:** 220–234

Allen DK, Ratcliffe RG (2009) Quantification of isotope label. *In* J Schwender, ed, Plant Metabolic Networks. Springer, New York, pp 105–149

Allen DK, Shachar-Hill Y, Ohlrogge JB (2007) Compartment-specific labeling information in ^{13}C metabolic flux analysis of plants. Phytochemistry **68:** 2197–2210

Almaas E, Kovacs B, Vicsek T, Oltvai ZN, Barabasi AL (2004) Global organization of metabolic fluxes in the bacterium *Escherichia coli*. Nature **427:** 839–843

Alonso AP, Goffman FD, Ohlrogge JB, Shachar-Hill Y (2007) Carbon conversion efficiency and central metabolic fluxes in developing sunflower (*Helianthus annuus* L.) embryos. Plant J **52:** 296–308

Antoniewicz MR, Kelleher JK, Stephanopoulos G (2007) Accurate assessment of amino acid mass isotopomer distributions for metabolic flux analysis. Anal Chem **79:** 7554–7559

Armstrong AF, Logan DC, Tobin AK, O'Toole P, Atkin OK (2006) Heterogeneity of plant mitochondrial responses underpinning respiratory acclimation to the cold in *Arabidopsis thaliana* leaves. Plant Cell Environ **29:** 940–949

Atkin OK, Macherel D (2009) The crucial role of plant mitochondria in orchestrating drought tolerance. Ann Bot (Lond) **103:** 581–597

Atkin OK, Tjoelker MG (2003) Thermal acclimation and the dynamic response of plant respiration to temperature. Trends Plant Sci **8:** 343–351

Becker SA, Palsson BO (2008) Context-specific metabolic networks are consistent with experiments. PLoS Comput Biol **4:** e1000082

Borodina I, Nielsen J (2005) From genomes to *in silico* cells via metabolic networks. Curr Opin Biotechnol **16:** 350–355

Boyer JS (1982) Plant productivity and environment. Science **218:** 443–448

Brand MD, Turner N, Ocloo A, Else PL, Hulbert AJ (2003) Proton conductance and fatty acyl composition of liver mitochondria correlates with body mass in birds. Biochem J **376:** 741–748

Brown GC, Lakin-Thomas PL, Brand MD (1990) Control of respiration and oxidative phosphorylation in isolated rat liver cells. Eur J Biochem **192:** 355–362

Chamberlin ME (2004) Top-down control analysis of the effect of temperature on ectotherm oxidative phosphorylation. Am J Physiol Regul Integr Comp Physiol **287:** R794–R800

Clifton R, Lister R, Parker KL, Sappl PG, Elhafez D, Millar AH, Day DA, Whelan J (2005) Stress-induced co-expression of alternative respiratory chain components in *Arabidopsis thaliana*. Plant Mol Biol **58:** 193–212

Covey-Crump EM, Attwood RG, Atkin OK (2002) Regulation of root respiration in two species of Plantago that differ in relative growth rate: the effect of short- and longterm changes in temperature. Plant Cell Environ **25:** 1501–1513

de Oliveira Dal'Molin CG, Quek LE, Palfreyman RW, Brumbley SM, Nielsen LK (2010) AraGEM, a genome-scale reconstruction of the primary metabolic network in Arabidopsis. Plant Physiol **152:** 579–589

Farre EM, Tiessen A, Roessner U, Geigenberger P, Trethewey RN, Willmitzer L (2001) Analysis of the compartmentation of glycolytic intermediates, nucleotides, sugars, organic acids, amino acids, and sugar alcohols in potato tubers using a nonaqueous fractionation method. Plant Physiol **127:** 685–700

Galle A, Florez-Sarasa I, Thameur A, de Paepe R, Flexas J, Ribas-Carbo M (2010) Effects of drought stress and subsequent rewatering on photosynthetic and respiratory pathways in *Nicotiana sylvestris* wild type and the mitochondrial complex I-deficient CMSII mutant. J Exp Bot **61:** 765–775

Gonzalez-Meler MA, Ribas-Carbo M, Giles L, Siedow JN (1999) The effect of growth and measurement temperature on the activity of the alternative respiratory pathway. Plant Physiol **120:** 765–772

Grafahrend-Belau E, Schreiber F, Koschutzki D, Junker BH (2009) Flux balance analysis of barley seeds: a computational approach to study systemic properties of central metabolism. Plant Physiol **149:** 585–598

Huege J, Sulpice R, Gibon Y, Lisec J, Koehl K, Kopka J (2007) GC-EI-TOF-MS analysis of *in vivo* carbon-partitioning into soluble metabolite pools of higher plants by monitoring isotope dilution after $^{13}CO_2$ labelling. Phytochemistry **68:** 2258–2272

Iyer VV, Sriram G, Fulton DB, Zhou R, Westgate ME, Shanks JV (2008) Metabolic flux maps comparing the effect of temperature on protein and oil biosynthesis in developing soybean cotyledons. Plant Cell Environ **31:** 506–517

Junker BH, Lonien J, Heady LE, Rogers A, Schwender J (2007) Parallel determination of enzyme activities and *in vivo* fluxes in *Brassica napus* embryos grown on organic or inorganic nitrogen source. Phytochemistry **68:** 2232–2242

Kopka J, Schauer N, Krueger S, Birkemeyer C, Usadel B, Bergmuller E, Dormann P, Weckwerth W, Gibon Y, Stitt M, et al (2005) GMD@CSB. DB: the Golm Metabolome Database. Bioinformatics **21:** 1635–1638

Kruger NJ, Ratcliffe RG (2009) Insights into plant metabolic networks from steady-state metabolic flux analysis. Biochimie **91:** 697–702

Kruger NJ, Troncoso-Ponce MA, Ratcliffe RG (2008) ^1H NMR metabolite fingerprinting and metabolomic analysis of perchloric acid extracts from plant tissues. Nat Protoc **3:** 1001–1012

Laine RA, Sweeley CC (1971) Analysis of trimethylsilyl O-methyloximes of carbohydrates by combined gas-liquid chromatography-mass spectrometry. Anal Biochem **43:** 533–538

Leimer KR, Rice RH, Gehrke CW (1977) Complete mass spectra of N-trifluoroacetyl-n-butyl esters of amino acids. J Chromatogr A **141:** 121–144

Libourel IGL, Shachar-Hill Y (2008) Metabolic flux analysis in plants: from intelligent design to rational engineering. Annu Rev Plant Biol **59:** 625–650

Lommen A (2009) MetAlign: interface-driven, versatile metabolomics tool for hyphenated full-scan mass spectrometry data preprocessing. Anal Chem **81:** 3079–3086

Lonien J, Schwender J (2009) Analysis of metabolic flux phenotypes for two Arabidopsis mutants with severe impairment in seed storage lipid synthesis. Plant Physiol **151:** 1617–1634

Masakapalli SK, Le Lay P, Huddleston JE, Pollock NL, Kruger NJ, Ratcliffe RG (2010) Subcellular flux analysis of central metabolism in a heterotrophic Arabidopsis cell suspension using steady-state stable isotope labeling. Plant Physiol **152:** 602–619

May M, Leaver C (1993) Oxidative stimulation of glutathione synthesis in *Arabidopsis thaliana* suspension cultures. Plant Physiol **103:** 621–627

Nantes IL, Fagian MM, Catisti R, Arruda P, Maia IG, Vercesi AE (1999) Low temperature and aging-promoted expression of PUMP in potato tuber mitochondria. FEBS Lett **457:** 103–106

Ndimba BK, Chivasa S, Simon WJ, Slabas AR (2005) Identification of Arabidopsis salt and osmotic stress responsive proteins using two-dimensional difference gel electrophoresis and mass spectrometry. Proteomics **5:** 4185–4196

Nielsen J, Villadsen J, Liden G (2003) Bioreaction Engineering Principles, Ed 2. Springer, New York

Piques M, Schulze WX, Hohne M, Usadel B, Gibon Y, Rohwer J, Stitt M (2009) Ribosome and transcript copy numbers, polysome occupancy and enzyme dynamics in Arabidopsis. Mol Syst Biol **5:** 314

Poolman MG, Miguet L, Sweetlove LJ, Fell DA (2009) A genome-scale metabolic model of Arabidopsis and some of its properties. Plant Physiol **151:** 1570–1581

Ratcliffe RG, Shachar-Hill Y (2006) Measuring multiple fluxes through plant metabolic networks. Plant J **45:** 490–511

Reed JL, Palsson BO (2003) Thirteen years of building constraint-based *in silico* models of *Escherichia coli*. J Bacteriol **185:** 2692–2699

Rolfe DF, Brand MD (1997) The physiological significance of mitochondrial proton leak in animal cells and tissues. Biosci Rep **17:** 9–16

Schuetz R, Kuepfer L, Sauer U (2007) Systematic evaluation of objective functions for predicting intracellular fluxes in *Escherichia coli*. Mol Syst Biol **3:** 119

Schwender J (2008) Metabolic flux analysis as a tool in metabolic engineering of plants. Curr Opin Biotechnol **19:** 131–137

Schwender J, Shachar-Hill Y, Ohlrogge JB (2006) Mitochondrial metabolism in developing embryos of *Brassica napus*. J Biol Chem **281:** 34040–34047

Seki M, Umezawa T, Urano K, Shinozaki K (2007) Regulatory metabolic networks in drought stress responses. Curr Opin Plant Biol **10:** 296–302

Skirycz A, De Bodt S, Obata T, De Clercq I, Claeys H, De Rycke R, Andriankaja M, Van Aken O, Van Breusegem F, Fernie AR, et al (2010) Developmental stage specificity and the role of mitochondrial metabolism in the response of Arabidopsis leaves to prolonged mild osmotic stress. Plant Physiol **152:** 226–244

Sriram G, Fulton DB, Iyer VV, Peterson JM, Zhou R, Westgate ME, Spalding MH, Shanks JV (2004) Quantification of compartmented metabolic fluxes in developing soybean embryos by employing biosynthetically directed fractional ^{13}C labeling, two-dimensional [^{13}C, ^1H] nuclear magnetic resonance, and comprehensive isotopomer balancing. Plant Physiol **136:** 3043–3057

Sriram G, Fulton DB, Shanks JV (2007) Flux quantification in central carbon metabolism of *Catharanthus roseus* hairy roots by ^{13}C labeling and comprehensive bondomer balancing. Phytochemistry **68:** 2243–2257

Sweetlove LJ, Burrell MM, apRees T (1996) Starch metabolism in tubers of transgenic potato (Solanum tuberosum) with increased ADPglucose pyrophosphorylase. Biochem J **320:** 493–498

Wahl SA, Dauner M, Wiechert W (2004) New tools for mass isotopomer data evaluation in (13)C flux analysis: mass isotope correction, data consistency checking, and precursor relationships. Biotechnol Bioeng **85:** 259–268

Wiechert W, Mollney M, Petersen S, de Graaf AA (2001) A universal framework for ^{13}C metabolic flux analysis. Metab Eng **3:** 265–283

Williams TCR, Miguet L, Masakapalli SK, Kruger NJ, Sweetlove LJ, Ratcliffe RG (2008) Metabolic network fluxes in heterotrophic Arabidopsis cells: stability of the flux distribution under different oxygenation conditions. Plant Physiol **148:** 704–718